

Multiple microcracking behavior of ultra-high-performance fiber-reinforced concrete under high-rate direct tension: Investigation based on a digital image correlation technique

Seoung Ik CHOI¹⁾, Min Kyoung KIM²⁾, *Dong Joo Kim³⁾ and Yun-Kyu AN⁴⁾

¹⁾ *Costal Development and Ocean Energy Research center, Korea Institute of Ocean Science and Technology, 385, Haeyang-ro, Yeongdo-gu, Busan, 49111, Korea / Department of Civil and Environmental Engineering, SEJONG University, 209, Neungdong-ro, Gwangjin-Gu, Seoul, 05006, Korea*

^{2), 3)} *Department of Civil and Environmental Engineering, SEJONG University, 209, Neungdong-ro, Gwangjin-Gu, Seoul, 05006, Korea*

⁴⁾ *Department of Architectural Engineering, SEJONG University, 209, Neungdong-ro, Gwangjin-Gu, Seoul, 05006, Republic of Korea*

³⁾ djkim75@sejong.ac.kr

ABSTRACT

This study investigated the multiple microcracking responses of ultra-high-performance fiber-reinforced concrete (UHPFRC) under tension. The digital image correlation (DIC) technique was applied to identify the location and calculate the width of the microcracks. Multiple microcracks were generated randomly under both static and high strain rates during tensile strain-hardening response. Microcrack width increased until the point of post-cracking tensile strength; then, the microcrack width was maintained or it decreased slightly as a major crack opened. The energy absorption capacity of UHPFRC at high strain rates was concluded to originate from the wider openings of microcracks at high strain rates.

1. INTRODUCTION

Ultra-high-performance fiber-reinforced concrete (UHPFRC) is considered highly favorable for robust and durable civil infrastructure based on its superior material properties that include high tensile strength and high energy absorption capacity [Thomas 2017, Naaman 1996]. The superior material properties of UHPFRC are based on its strain-hardening response that is accompanied by multiple microcracks under direct tension [Park 2012]. The energy absorption capacity of UHPFRC is correlated

¹⁾ Master (M.S)

²⁾ Graduate Student (Ph.D candidate)

³⁾ Professor

⁴⁾ Associate Professor

with its strain capacity and tensile strength, and the strain capacity can be increased by higher numbers of multiple microcracks with wider width [Wille 2014]. Thus, to enhance the energy absorption capacity of UHPFRC, especially at high strain rates, the response of multiple microcracks must be clearly understood.

Many researchers have reported on the multiple microcracking responses of UHPFRC under direct tension at both static and higher strain rates [Tran 2014, Tran 2015, Park 2016, Park 2017]. For example, Tran (2015) reported rate-sensitive tensile responses of UHPFRC, although their sensitivity analysis was dependent on the type of fibers. They found that the number of multiple microcracks increased and that the strain capacity of UHPFRC increased as the strain rate increased from static (0.0001671 s^{-1}) to high strain rates (23.4 s^{-1}). However, they did not provide direct information on microcrack width. Based on the strain capacity and the number of microcracks of UHPFRC, Park (2017) calculated the average microcrack width at the point of post-cracking strength corresponding to different matrices and strain rates. They concluded that the width of multiple microcracks increased as the strain rate increased.

Current information regarding the microcracking responses of UHPFRC is based mostly on indirect measurement technology. Various methods have been used to measure the location and width of microcracks, e.g., strain gauges, linear variable differential transformers (LVDTs), and clip gauges. Strain gauges measure the strain only within the elastic limit and therefore they cannot measure crack width when the gauges are damaged by cracking. Similarly, LVDTs cannot measure the width of cracks exactly, while clip gauges are applicable only for predetermined crack locations. Thus, it remains very difficult to observe and monitor the location and width of multiple microcracks of UHPFRC under load.

This study applied a digital image correlation (DIC) technique to understand the multiple microcracking responses of UHPFRC under tension at both static and high strain rates. An improved strain energy impact test machine (I-SEFIM) was used in higher strain rate tensile tests [Park 2016, Park 2017]. The detailed objectives of the study were 1) to investigate the process of generating multiple microcracks in UHPFRC during direct tensile tests, 2) to investigate the effects of high strain rate on the microcracking process and the number of cracks, and 3) to observe the changes in the width of multiple microcracks during the tests.

2. DIGITAL IMAGE CORRELATION TECHNIQUE IN CONCRETE ENGINEERING

DIC technology has been used widely in experimental mechanics as well as concrete engineering in numerous studies. For example, DIC technology has been applied to investigate the global behavior of structural members and structures [Chu 1985, Destrebeeq 2011, Gencturk 2014]. Chu (1985) applied DIC to determine the centerline displacements of a cantilever beam. Destrebeeq (2011) applied DIC for the determination of the actual mechanical behavior of a full-scale reinforced concrete beam after its 25 years' service in a severe industrial environment. They concluded that the DIC technique was suitable for early crack detection and measurement. Gencturk (2014) also applied the DIC technique to measure the strain of prestressed concrete structures under full-scale tests.

DIC technology has also been used to investigate the fracture process of concrete [Choi 1997, Yoneyama 2006, Shah 2011, Wu 2011, Choi 2012]. Choi (1997) developed a nondestructive displacement evaluation system using a digital image cross-correlation scheme and computer vision to perform microscopic examination of the fracture processes in concrete under compression. Yoneyama (2006) studied a method for determining mixed-mode stress intensity factors from displacement fields obtained by DIC. Shah (2011) investigated the fracture properties of concrete and concrete interfaces using DIC. They reported that crack mouth opening displacement and vertical load-point displacement computed using DIC analysis matched well with experimental measurements. Wu (2011) also investigated the properties of a fracture process zone in concrete using the DIC technique and they reported that the length of the fracture process zone increased as the specimen height increased. Choi (2012) applied DIC to measure the width of cracks at notched/unnotched regions of concrete.

DIC technology has been used successfully to investigate crack propagation in cement-based materials at high rate tests [Forquin 2012, Gao 2015, Pyo 2016]. Forquin (2012) developed “the rocking spalling test” and applied the DIC technique to investigate the crack-propagation velocity in concrete and rock-like materials under dynamic tensile loading. Gao (2015) investigated the rate dependence of fracture propagation in rocks using DIC in notched semicircular bending tests at high rates. Pyo (2016) also investigated crack propagation in ultra-high-performance concrete (UHPC) under a wide range of loading rates using DIC.

3. EXPERIMENTAL PROGRAM

An experimental program was designed to investigate the multiple microcracking responses of UHPFRC under tension at both static and higher strain rates, and to determine whether different strain rates generate significant effects on the width and number of multiple microcracks. Four series of direct tensile specimens of UHPFRC containing 0.5–2.0 vol% steel fibers were tested at both static (0.000333 s^{-1}) and high ($40.3\text{--}90.0 \text{ s}^{-1}$) strain rates.

3.1 Material properties and specimen preparation

Smooth straight steel fibers were added to samples of UHPC. The properties of the high-strength steel fibers are provided in Table 1, and the matrix composition and compressive strength of the UHPC are given in Table 2. A Hobart mortar mixer with 20-L capacity was used to prepare the experimental specimens. Silica sand and silica fume were first added and dry mixed for 5 min. Subsequently, cement and silica powder were added and mixing continued for a further 10 min. After the dry mixing was complete, water and a superplasticizer were added in sequence. The mixture was then

Table 1 Properties of high-strength steel fibers

Notation	Diameter (mm)	Length (mm)	Density (g/cm^3)	Tensile strength (MPa)	Elastic modulus (GPa)
Smooth fiber	0.2	19.5	7.9	2788	200

Table 2 – Matrix composition by weight ratio and compressive strength

Cement (Type)	Silica sand	Silica fume	Silica powder	Super- plasticizer	Water	f_c' (MPa)
1.00 (I)	1.10	0.25	0.30	0.067	0.20	180

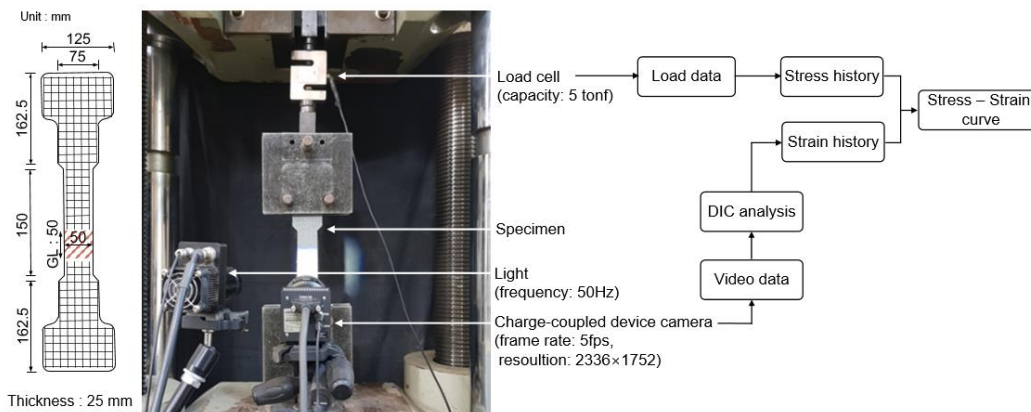
mixed for a further 5 min. When the mixed mortar showed suitable flow capability and viscosity for uniform fiber distribution, the fibers were dispersed carefully by hand into the mortar mixture.

3.2 Test setup and procedure

The geometry of the specimen and test setup for the static and high rate tensile strain tests are illustrated in Fig. 1a and 1b, respectively. The width and thickness of each specimen was 50 and 25 mm, respectively. The gauge length for measuring the tensile elongation of the specimens was 50 mm. A universal testing machine running in displacement control was used to conduct the static tensile tests. The speed of displacement during the static tensile tests was 1.0 mm/min. The I-SEFIM was used to conduct the high rate tensile tests.

During the static tensile tests, the load signal was measured by the load cell with 5 tonf capacity, while the tensile elongation was obtained using the DIC technique. A charge-coupled device camera was used to record sequential images with resolution of 2336 × 1752 pixels at the frequency of 5 Hz. During the high rate tensile tests, the load signal was obtained by averaging the signal from two strain gauges attached on either side of the transmitter bar in the I-SEFIM, as shown in Fig. 1b. A high-speed camera system was used to capture sequential images with resolution of 256 × 128 pixels at the frequency of 50 kHz. A high-frequency light system was used during the tests. Detailed information about the procedure of the high rate tensile tests can be found in Park (2016).

The mortar mixture incorporating the fibers was placed carefully (to avoid vibration) in a mold using a scoop. Two layers of steel wire mesh were added to both ends of each specimen for reinforcement. After casting, the specimens were covered by plastic sheeting and placed at room temperature in a laboratory for 48 h prior to



(a) Static tensile test set-up (0.000333 s⁻¹)

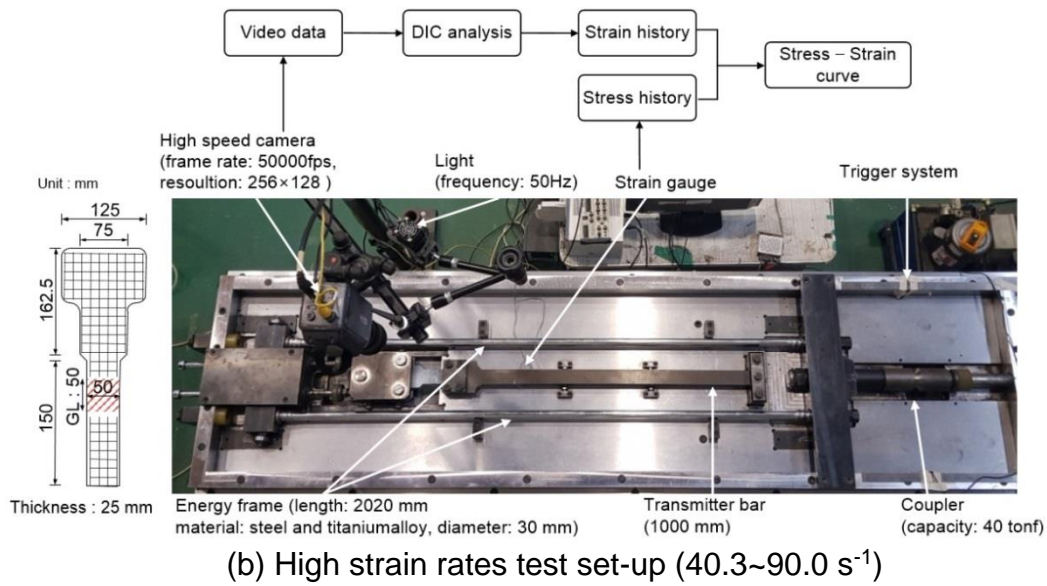


Fig. 1 Specimen geometry and setup for direct tensile test

demolding. Then, the specimens were cured in water at 90 °C for 3 d. Subsequently, the specimens were dried and stone powder was sprayed onto the surface of those specimens intended for the static tensile tests, whereas random speckles were sprayed onto the surface of those specimens intended for the high rate tensile tests.

3.3 Subset size

The accuracy of DIC analysis is affected by the subset size, which directly determines the area used for tracking of the displacement between the reference and target subsets. Subset size is known to be critical regarding the accuracy of measured displacement [Yaofeng 2007]. Pan (2008) proposed the sum of square of subset intensity gradient (SSSIG) as a useful parameter for determining an appropriate subset size by considering inherent image noise. Factors that determine the suitable subset size include the SSSIG value, standard deviation error, and image variance. The relationship between the SSSIG value and the standard deviation error can be expressed as follows [Pan 2008]:

$$\sigma(\Delta u) \approx \left[\frac{D(\eta)}{\sum_{x=-M}^{x=M} \sum_{y=-M}^{y=M} (f_x)^2} \right]^{1/2}$$

$$\sigma(\Delta v) \approx \left[\frac{D(\eta)}{\sum_{x=-M}^{x=M} \sum_{y=-M}^{y=M} (f_y)^2} \right]^{1/2} \quad (1)$$

where x, y are the coordinates in both the reference and the deformed images; M is the selected subset size in pixels; f_x, f_y are the first-order derivatives of the grayscale intensities that are calculated using the central difference of neighboring points in the x, y directions; $\Delta u, \Delta v$ are the corresponding subpixel displacements in the x, y directions; $D(\eta)$ is the variance of image noise; and,

$$\sum_{x=-M}^{x=M} \sum_{y=-M}^{y=M} (f_x)^2 \quad \text{and} \quad \sum_{x=-M}^{x=M} \sum_{y=-M}^{y=M} (f_y)^2 \quad \text{are the SSSIG values.}$$

The subset size can be determined by following the procedure described in Fig. 2. The target standard deviation error (α) should be set at the beginning. The variance of image noise ($D(\eta)$) can be calculated using MATLAB code. Then, the subset size in pixels $(2M + 1) \times (2M + 1)$ can be assumed and the SSSIG values ($\sum_{x=-M}^{x=M} \sum_{y=-M}^{y=M} (f_x)^2$ and $\sum_{x=-M}^{x=M} \sum_{y=-M}^{y=M} (f_y)^2$) calculated. Through the use of the variance of image noise and the SSSIG values, the standard deviation error values ($\sigma(\Delta u), \sigma(\Delta v)$) can be calculated using Eq. (1). If the standard deviation error values are higher than α , then M is reassumed to be $M + 1$ and $M + 1$. This process is repeated until the standard deviation error is less than α . After determining the suitable subset size, the DIC analysis can be performed.

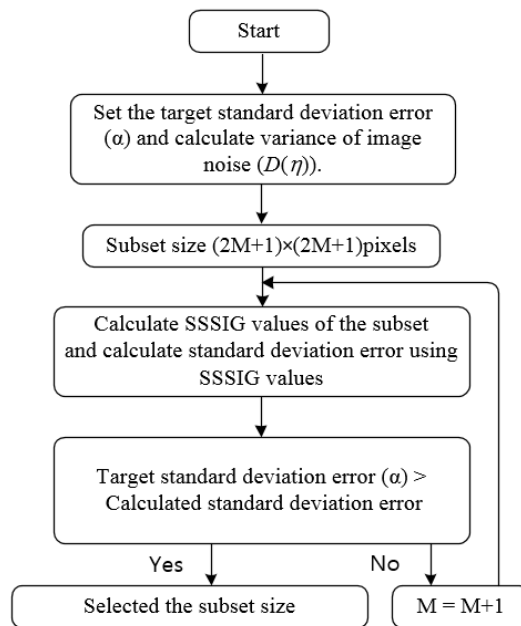
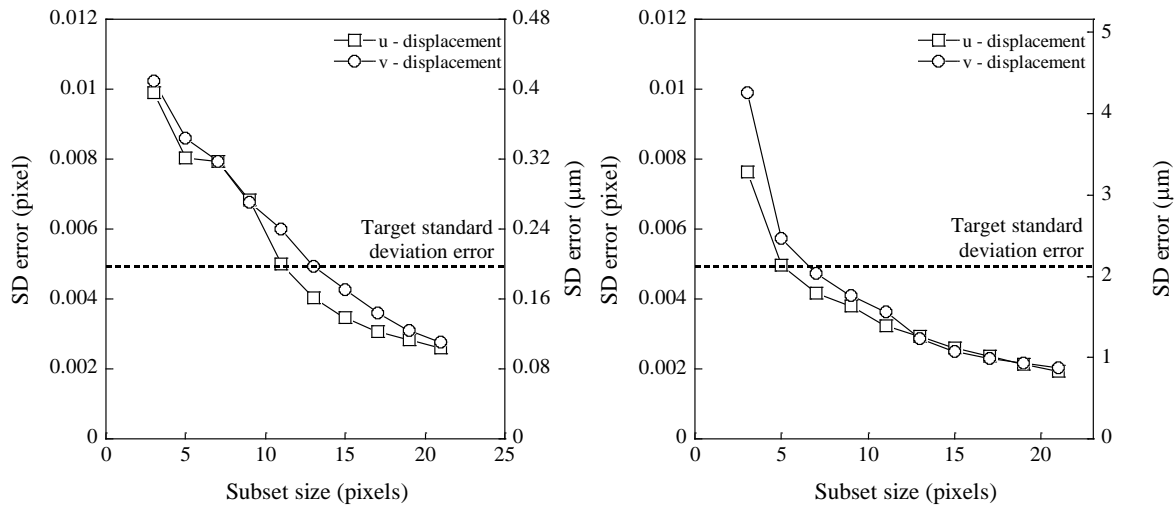


Fig. 2 Flowchart of the algorithm for optimal selection of subset size [Pan 2008]

In this study, the value of α was selected as 0.005. The variance of image noise ($D(\eta)$) was obtained as 6.0 and 2.6 at static and high strain rates, respectively. The correlation between the standard deviation error and the subset size for the static and high strain rates is shown in Fig. 3a and 3b, respectively, while Table 3 summarizes their values. It can be seen that the SSSIG value increased as the subset size increased, whereas the standard deviation error clearly decreased. To satisfy α , as can be seen in both Table 3 and Fig. 3, the subset size was selected as 15×15 pixels

(actual size per pixel = 40 μm) at the static strain rate and 7 \times 7 pixels (actual size per pixel = 430 μm) at the high strain rates, respectively. The standard deviation errors ($\sigma(\Delta u)$, $\sigma(\Delta v)$) were 0.0035 and 0.0043 pixel (0.14 and 0.17 μm) at the static strain rate and 0.0041 and 0.0047 pixel (1.76 and 2.02 μm) at the high strain rates, respectively.



(a) Static strain rate (Noise variance = 6.0) (b) High strain rate (Noise variance = 2.6)

Fig. 3 Standard deviation of displacement

Table 3 Standard deviation error corresponding to strain rates

Strain rate	Direction	Subset size (pixels)									
		3	5	7	9	11	13	15	17	19	
Static rate	x	SSSIG ^a	45020	69839	111095	205660	287580	358264	449369	568651	684531
		SD ^b error	0.011540	0.009260	0.007350	0.005400	0.004570	0.004090	0.003650	0.003250	0.00296
	y	SSSIG	57277	80732	95285	130188	167265	238573	328065	464912	625975
		SD error	0.010230	0.008620	0.007930	0.006790	0.005990	0.005010	0.004270	0.003590	0.00309
High strain rates	x	SSSIG	44423	104424	149582	178152	248211	302013	382851	465181	562011
		SD error	0.007640	0.004980	0.004160	0.003810	0.003230	0.002930	0.002600	0.002360	0.00215
	y	SSSIG	26418	78479	114909	153725	195761	314663	418758	483011	551469
		SD error	0.0099	0.005740	0.004750	0.004100	0.003640	0.002870	0.002490	0.002320	0.00217

^a : sum of square of subset intensity gradients

^b : standard deviation

The effects of different subset sizes on the results of the DIC analysis at static and high strain rates are shown in Figs. 4 and 5, respectively. The suitable subset size was 15 \times 15 pixels (Fig. 4b) at the static strain rate and 7 \times 7 pixels (Fig. 5b) at high

strain rates. When the subset size was 10×10 pixels (Fig. 4a) at the static strain rate and 5×5 pixels (Fig. 5a) at the high strain rates, it was difficult to recognize microcracks. Conversely, when the subset size was 20×20 pixels (Fig. 4c) at the static strain rate and 9×9 pixels (Fig. 5c) at high strain rates, microcrack width was slightly overestimated.

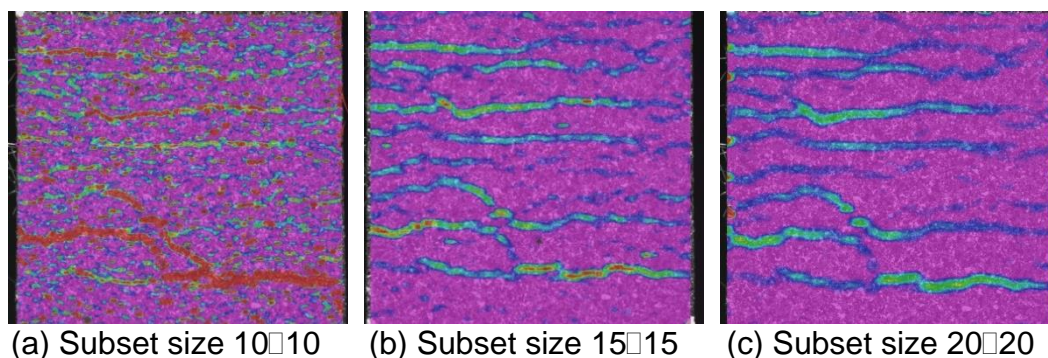


Fig. 4 The effect of subset size on DIC analysis at static strain rate

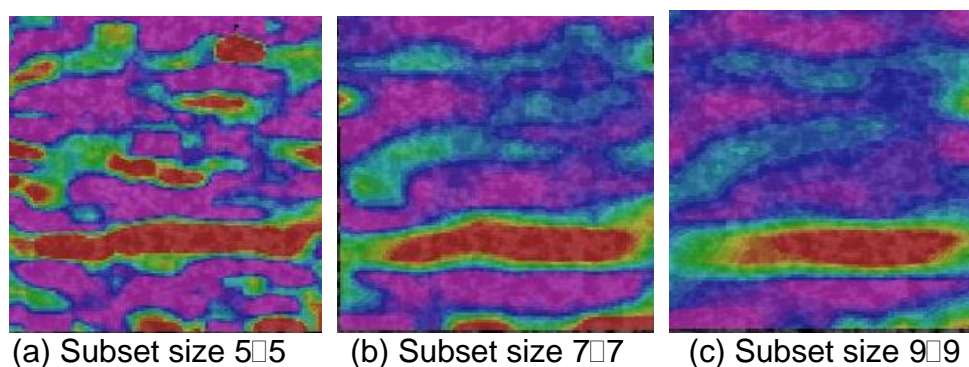
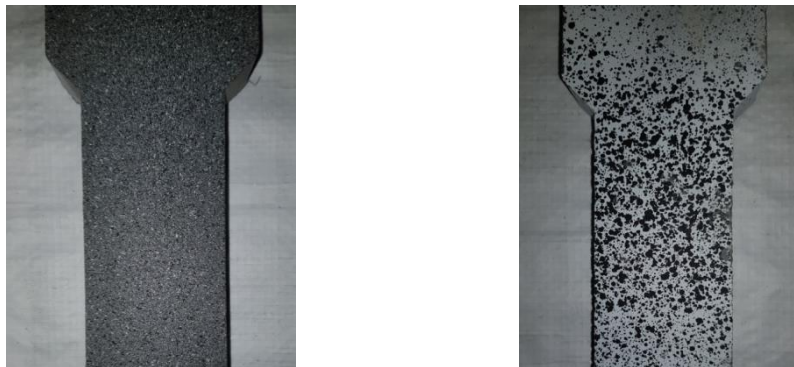


Fig. 5 The effect of subset size on DIC analysis at high strain rates

3.4 DIC analysis

The surface treatments of the specimens used for the DIC analysis are shown in Fig. 6. Different treatments were applied to the surface of specimens corresponding to the applied strain rates. Coarser random speckles were applied to the surface of specimens used for the high rate tensile tests. This was because the resolution of the images of the specimens subjected to the high strain rate tensile tests was much lower than that of the images of the specimens subjected to the static tests.

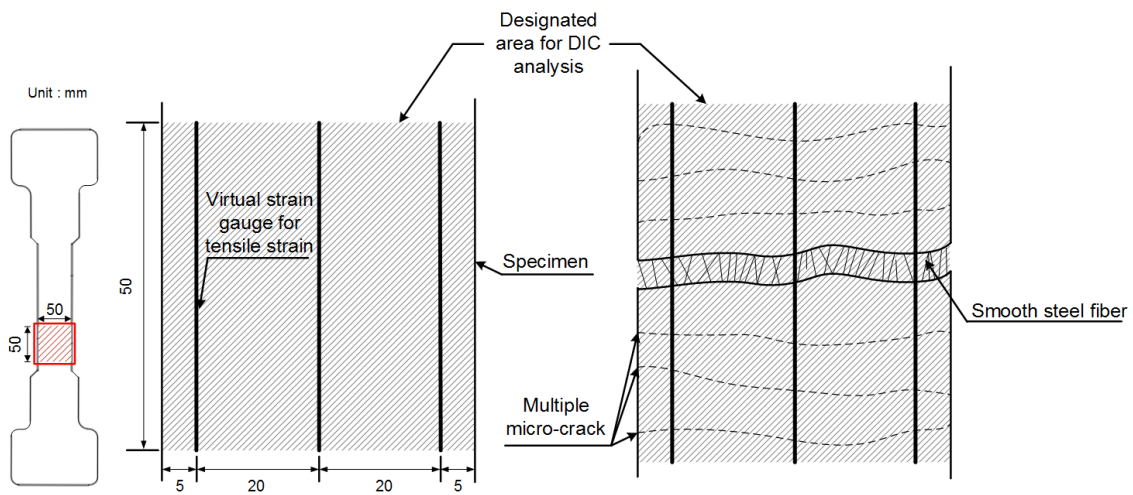
The locations of the virtual strain and crack gauges used in the DIC analysis are illustrated in Fig. 7. Three virtual strain gauges were used for measuring the tensile elongation within a 50-mm gauge length (Fig. 7a). The history of tensile elongation could be calculated by averaging the signals from the three virtual strain gauges. Virtual crack gauges were used to estimate microcrack width. The gauges used for crack width were located in the middle of each specimen and the length of the crack gauge was selected as 4 mm, as can be seen in Fig. 7.



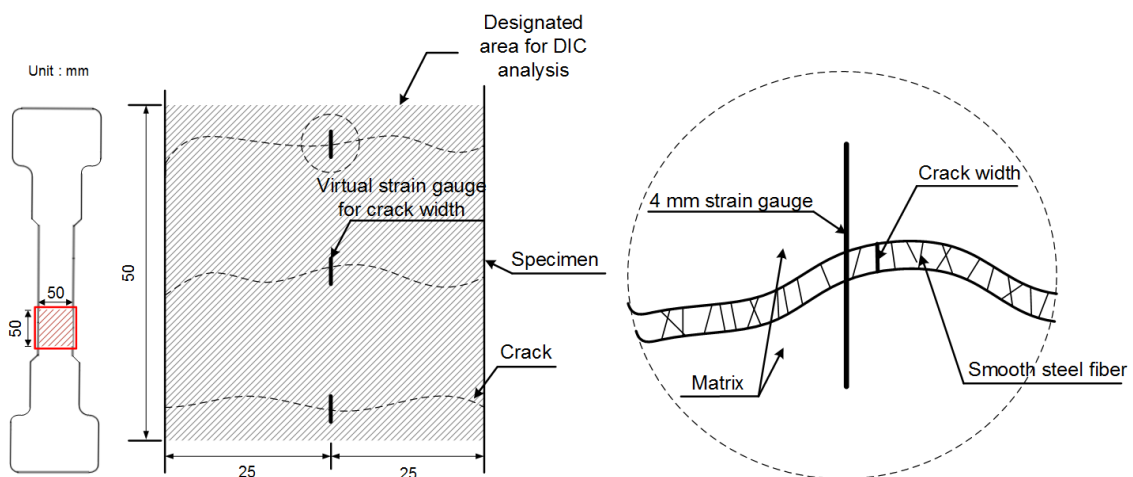
(a) Stone power sprayed on the surface of specimens at static strain rate

(b) Speckles sprayed on the surface of specimens at high strain rates

Fig. 6 Surface treatments for DIC analysis



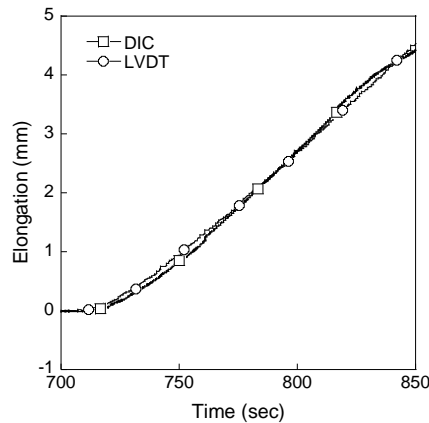
(a) Virtual strain gauges within gauge length



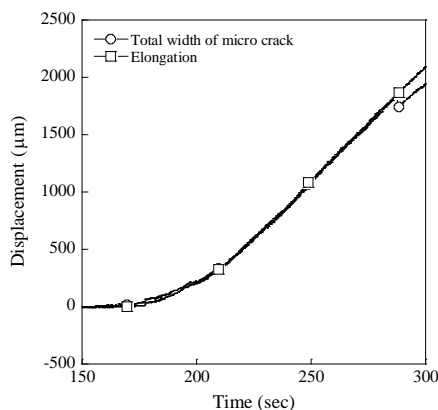
(b) Virtual crack gauge for measuring the width of crack

Fig. 7 Virtual strain gauges used in the DIC analysis

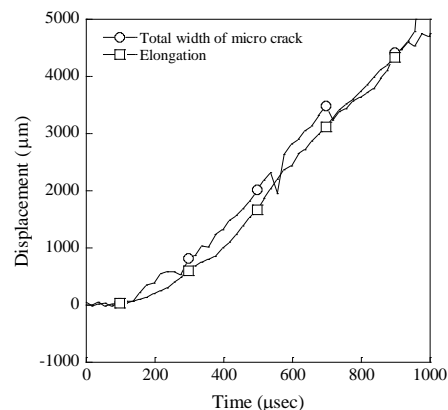
The validity of using DIC analysis to estimate tensile elongation was verified by comparing the results with the elongation measured using two LVDTs (Fig. 8a). Furthermore, Fig. 8b and 8c also compare the tensile elongation measured by the virtual strain gauges in Fig. 7a and the summation of microcrack width measured by the virtual crack gauges in Fig. 7b. The test results at the static rate coincided well, as can be seen in Fig. 8b. However, at high strain rates, the summation of microcrack widths obtained from the virtual crack gauges was found slightly higher than the tensile elongation measured by the virtual strain gauges, as can be seen in Fig. 8c.



(a) Validation of using virtual strain gauges



(b) Validation of using virtual crack gauges at static strain rate (0.0003333s^{-1})



(c) Validation of using virtual crack gauges at high strain rates ($(40.3\sim90.0\text{ s}^{-1})$)

Fig. 8 Validation of using virtual strain gauges in DIC analysis

4. TEST RESULTS

The tensile parameters (post-cracking strength, strain capacity, peak toughness, and number of multiple cracks) of UHPFRC measured at both static and high strain rates are summarized in Table 4. The post-cracking strength is the maximum tensile stress, whereas the strain capacity is the strain value at the point of post-cracking strength. Peak toughness is the area under the tensile stress–strain curve until the

post-cracking point. In this study, the number of microcracks was counted based on the results of the DIC analysis. Total crack length was calculated using the DIC program and the number of cracks was calculated by dividing the total crack length by the specimen width.

Table 4 Tensile parameters of UHPFRCs

Test series	Strain rate	Rate (s ⁻¹)	Specimen	Post cracking strength		Strain capacity		Peak toughness		Number of multiple cracks	
				MPa	DIF	%	DIF	kJ/m ³	DIF	ea	DIF
S0.5	Static	0.000333	SP1	6.18	-	0.217	-	11.97	-	1.0	-
			SP2	4.95	-	0.124	-	4.97	-	1.0	-
			SP3	5.03	-	0.182	-	8.11	-	1.0	-
			Average	5.34	1.0	0.217	1.0	8.35	1.0	1.0	1.0
I0.5	High strain rate	54.87	SP1	20.34	3.84	0.676	3.12	112.35	13.46	2.2	2.2
			SP2	19.23	3.60	0.602	4.85	126.37	15.13	1.5	1.5
			SP3	20.38	3.81	1.025	4.72	161.83	19.38	2.7	2.7
S1.0	Static	0.000333	SP1	9.33	-	0.379	-	35.81	-	2.6	-
			SP2	9.11	-	0.225	-	18.54	-	1.5	-
			SP3	10.60	-	0.504	-	51.47	-	3.1	-
			Average	9.60	1.0	0.369	1.0	27.58	1.0	2.4	1.0
I1.0	High strain rate	64.13	SP1	20.44	2.13	0.974	2.57	181.35	6.58	3.8	1.58
			SP2	22.41	2.33	0.765	2.07	181.41	6.58	4.7	1.96
			SP3	23.34	2.43	0.522	1.41	148.52	5.39	4.2	1.75
S1.5	Static	0.000333	SP1	13.70	-	0.720	-	84.94	-	6.3	-
			SP2	12.54	-	0.881	-	100.05	-	6.2	-
			SP3	12.74	-	0.681	-	82.08	-	4.2	-
			Average	12.91	1.0	0.761	1.0	87.36	1.0	5.6	1.0
I1.5	High strain rate	68.65	SP1	32.12	2.48	0.891	1.17	266.97	3.06	5.4	0.96
			SP2	28.85	2.23	0.651	0.85	176.28	2.02	6.6	1.18
			SP3	33.74	2.61	0.563	0.74	175.30	2.01	6.1	1.09
			SP4	32.09	2.48	0.815	1.07	185.27	2.12	5.2	0.93
S2.0	Static	0.000333	SP1	15.08	-	0.852	-	114.15	-	9.6	-
			SP2	14.70	-	0.625	-	87.92	-	7.4	-
			SP3	13.28	-	0.903	-	107.01	-	4.2	-
			Average	14.29	1.0	0.793	1.0	99.82	1.0	7.1	1.0
I2.0	High strain rate	82.36	SP1	40.52	2.84	0.809	1.02	392.45	3.93	6.7	0.97
			SP2	46.62	3.26	0.655	0.83	358.13	3.59	6.4	1.10
			SP3	37.12	2.59	1.35	1.70	421.62	4.22	5.9	1.06
			SP4	33.62	2.35	0.992	1.25	241.41	2.42	5.7	0.89

The tensile stress versus strain curves of UHPFRC containing 0.5–2.0 vol% short steel fibers at the static strain rate are shown in Fig. 9. All samples of UHPFRC produced a tensile strain-hardening response. As the volume content of steel fibers

increased, both the post-cracking strength and the strain capacity of the UHPFRC increased. Based on the enhanced post-cracking strength and strain capacity, the peak toughness of the UHPFRC also increased notably from 8.35 to 99.82 kJ/m³ as the volume content of steel fiber increased from 0.5 to 2.0 vol%. The UHPFRC containing 0.5 vol% steel fibers produced a single major crack, whereas the UHPFRC containing 2.0 vol% steel fibers produced an average of seven microcracks.

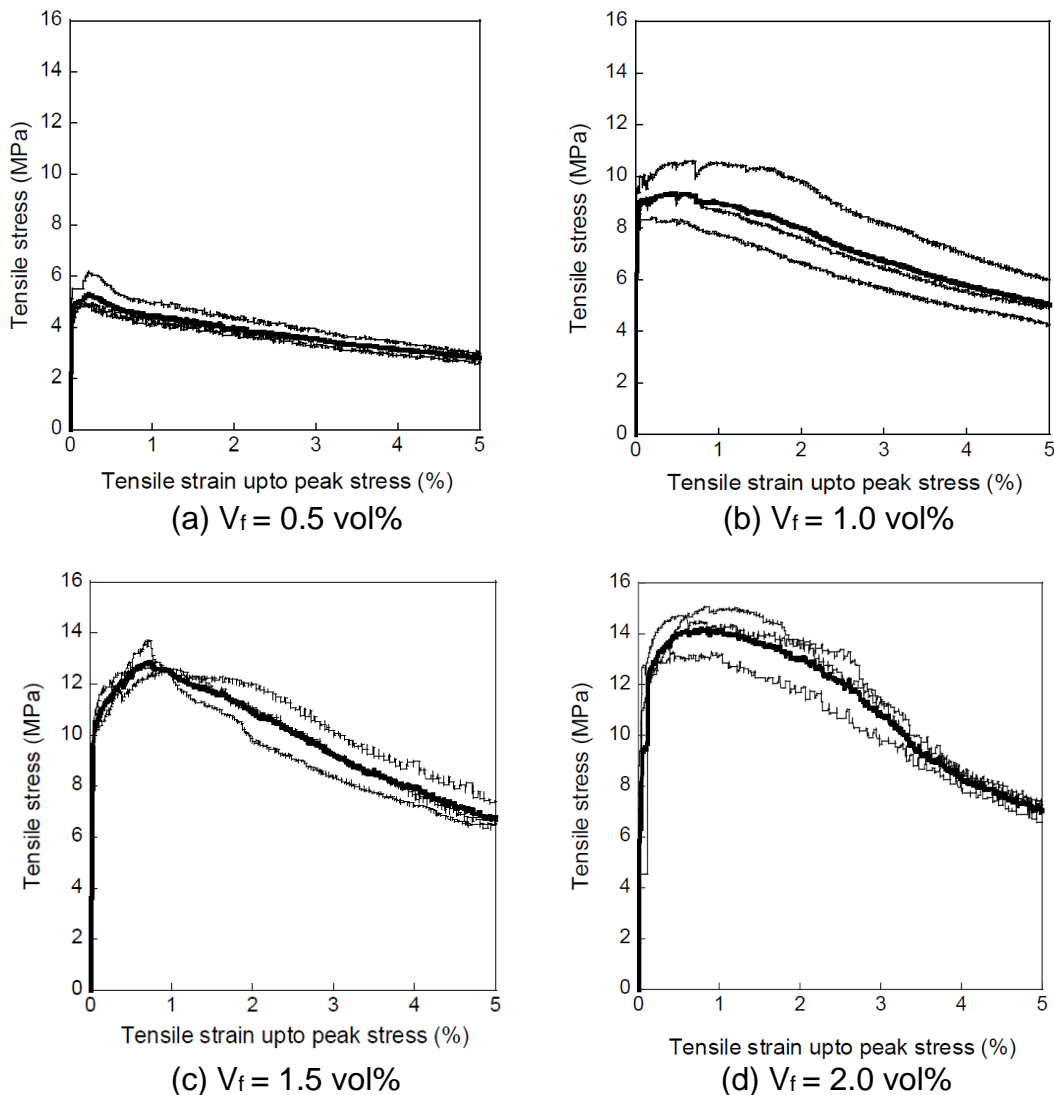


Fig. 9 Tensile stress versus strain responses of UHPFRCs at static strain rate

The tensile response of the UHPFRC at high strain rates of 40.3–90.0 s⁻¹ is shown in Fig. 10. The post-cracking strength of UHPFRC at high strain rates was 20.0, 22.0, 31.7, and 39.5 MPa, which corresponded to the volume content of steel fibers of 0.5, 1.0, 1.5, and 2.0 vol%, respectively. The UHPFRC with higher volume content of steel fibers clearly generated higher post-cracking strength in the static tensile tests. However, the UHPFRC with 0.5 vol% steel fibers produced the highest dynamic increase factor (DIF: 3.75).

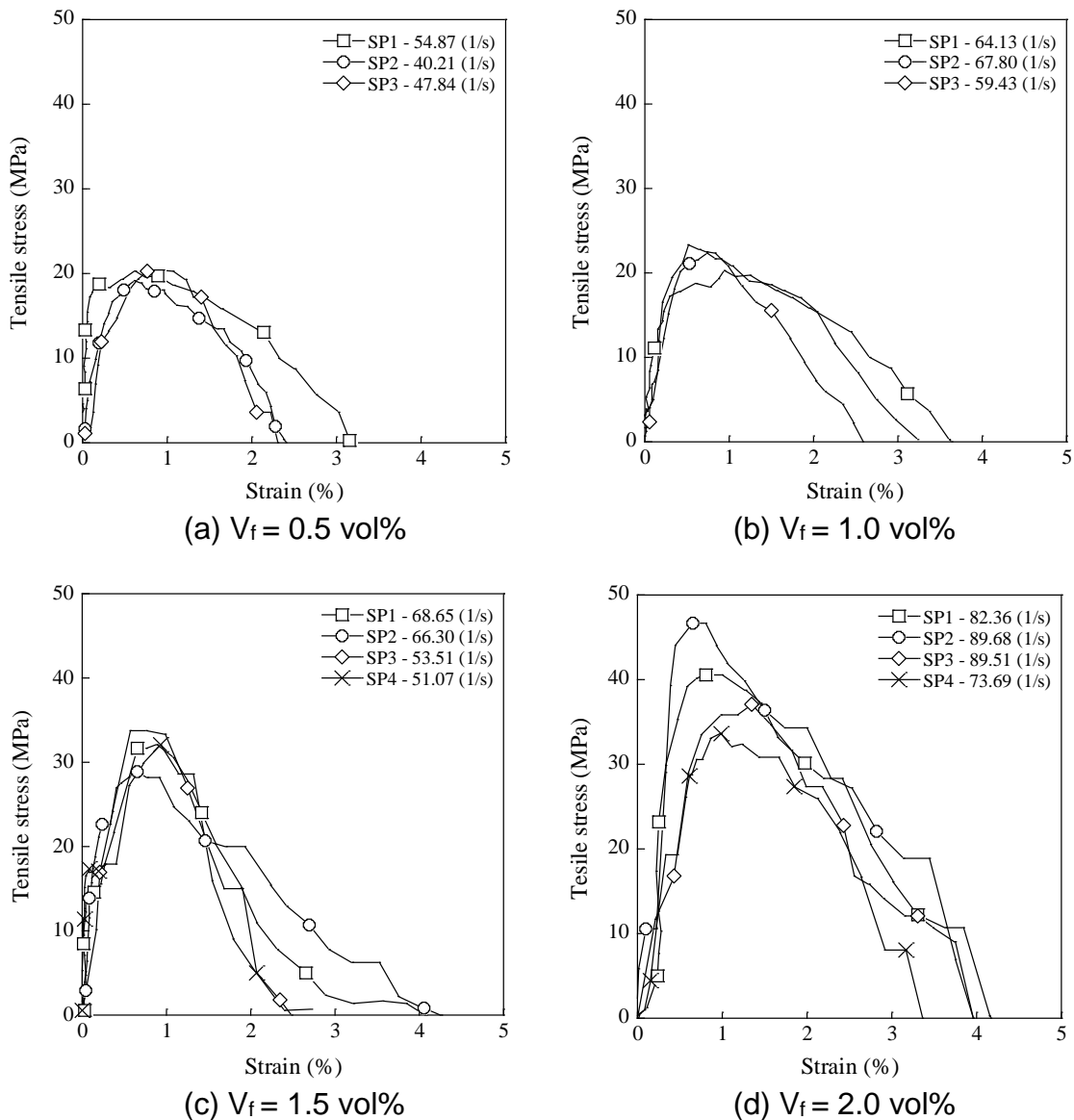


Fig. 10 Tensile stress versus strain responses of UHPFRCs at high strain rates

The number of microcracks at high strain rates also increased from 2.1 to 6.2 as the volume content of steel fibers increased from 0.5 to 2.0 vol%. Nevertheless, it was difficult to clearly recognize the high rate effect on the number of microcracks of the UHPFRC, especially in samples containing a volume content of steel fibers >1.5 vol%.

The DIF for the strain capacity of UHPFRC at high strain rates of 40.3–90.0 s^{-1} decreased as the volume content of fibers increased from 0.5 to 2.0 vol%. The DIFs for the strain capacity of UHPFRC containing 0.5 vol% steel fibers were 3.12 and 4.85, whereas those of UHPFRC with 2.0 vol% steel fibers were between 0.83 and 1.70. Consequently, the DIFs for the peak toughness of UHPFRC with lower fiber content were found higher, as summarized in Table 4, even though the peak toughness of UHPFRC with higher fiber content was generally higher than UHPFRC with lower fiber content.

5. DISCUSSION

5.1 Process of multiple microcracking of UHPFRC

Sequential images of UHPFRC with 2.0 vol% steel fibers under tension at the static strain rate (0.000333 s^{-1}) are shown in Fig. 11. It is clear that all the multiple microcracks of the UHPFRC are created prior to the post-cracking point. After the post-cracking point, no additional microcracks developed. The UHPFRC with lower fiber content generated faster crack percolation ($\Delta t = 2.2\text{--}15.2 \text{ s}$), whereas the UHPFRC with higher fiber content took longer ($\Delta t = 35.0\text{--}57.4 \text{ s}$) for the coalescence and percolation of microcracks. In the UHPFRC specimens with high fiber volume content, the DIC analysis revealed that multiple microcracks were partially created initially, which then developed later as percolated microcracks under tension.

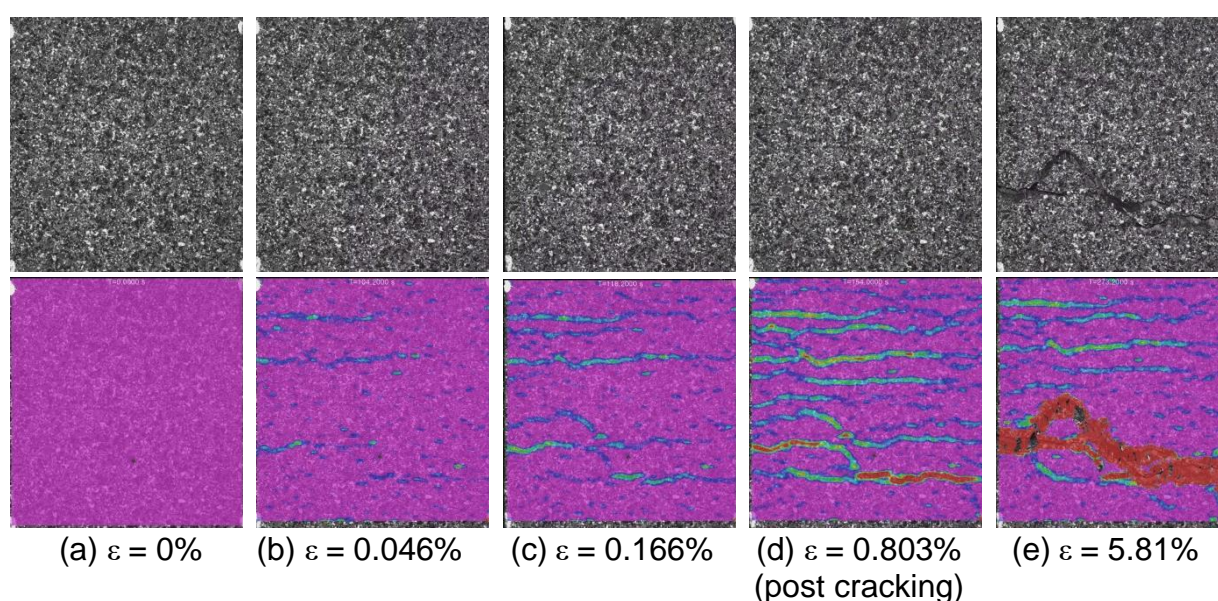


Fig. 11 Multiple microcracking response of UHPFRCs with 2.0 vol% steel fibers at static strain rate

5.2 High strain rate effects on multiple microcracking and the number of microcracks

Multiple microcracks of UHPFRC specimens under high rate tension were created in a very short period ($210 \mu\text{s}$; 2.0 vol%). Unlike the UHPFRC specimens under static strain rate, several instances of multiple microcracks were initiated and then developed as multiple percolated microcracks almost simultaneously at high strain rates of $40.3\text{--}90.0 \text{ s}^{-1}$, as can be seen in Fig. 12. Moreover, a greater number of multiple microcracks were generated at higher strain rates. However, the DIFs for the numbers of microcracks differed depending on the fiber volume content.

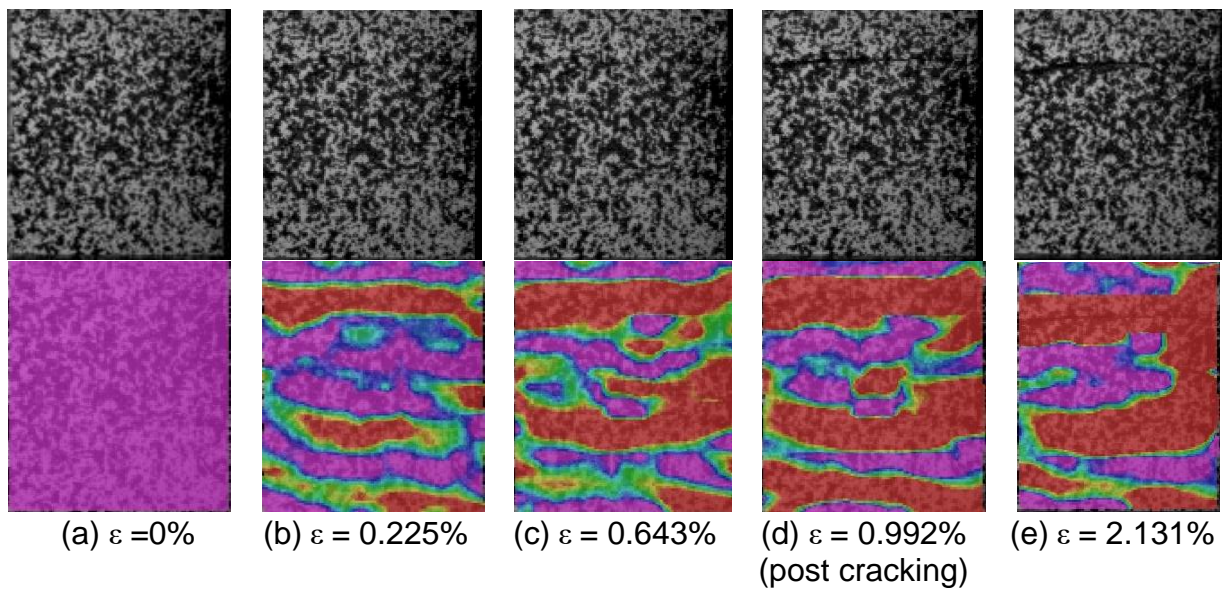


Fig. 12 Multiple microcracking response of UHPFRCs with 2.0 vol% steel fibers at high strain rates

5.3 History of multiple microcrack width of UHPFRC under tension

The history of microcrack width of UHPFRC under the static strain rate (0.000333 s^{-1}) is shown in Fig. 13a, while that of UHPFRC under high strain rates ($40.3\text{--}90.0 \text{ s}^{-1}$) is shown in Fig. 13b corresponding to the different steel fiber volume. During the tensile tests of UHPFRC containing 2.0 vol% steel fibers, the width ($114 \mu\text{m}$) of the multiple microcracks was generally higher at the higher strain rates ($40.3\text{--}90.0 \text{ s}^{-1}$) than at the static strain rate ($56 \mu\text{m}$; 0.000333 s^{-1}). It can be seen that microcrack width was maintained or it decreased slightly after major crack localization (Fig. 13a and 13b). The high strain rate effects on the average width of multiple microcracks at the post-cracking point are shown in Fig. 14.

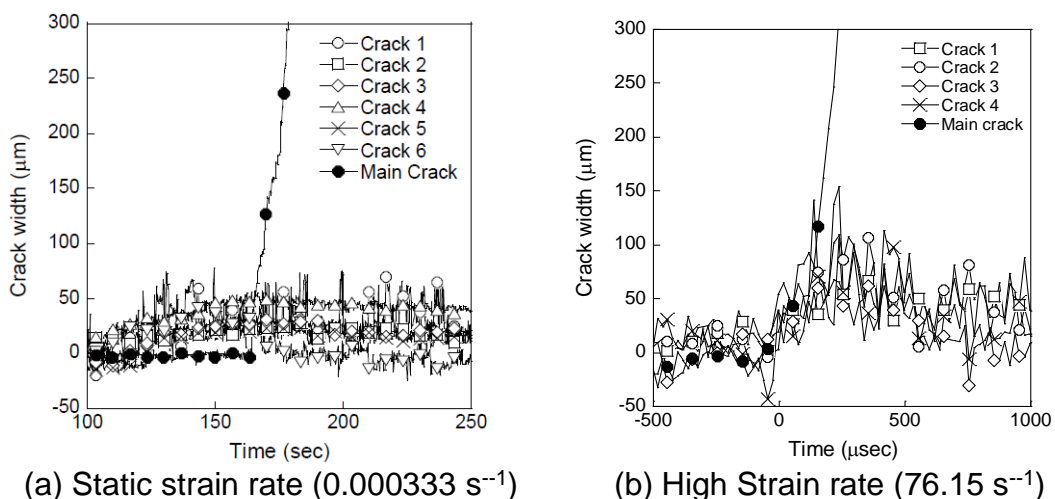


Fig. 13 Change in the width of multiple microcracks of UHPFRCs during static tensile test ($V_f = 2.0\%$)

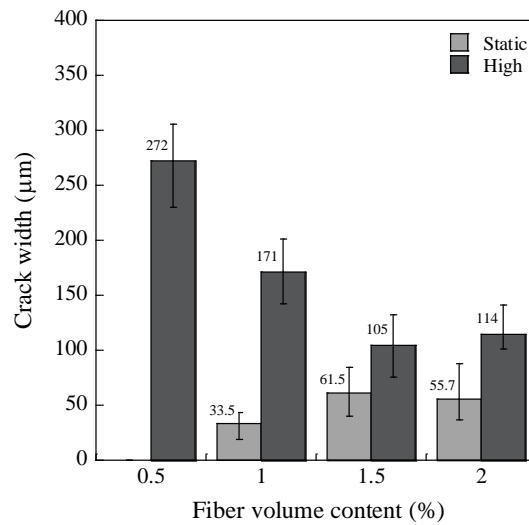


Fig. 14 High strain rate effect on the width of average width of multiple microcracks at post cracking point

The history of the summation of microcrack width of UHPFRC containing 2.0 vol% steel fibers under tension is illustrated in Fig. 15. It can be seen that the total width of the microcracks was maximized at the post-cracking point.

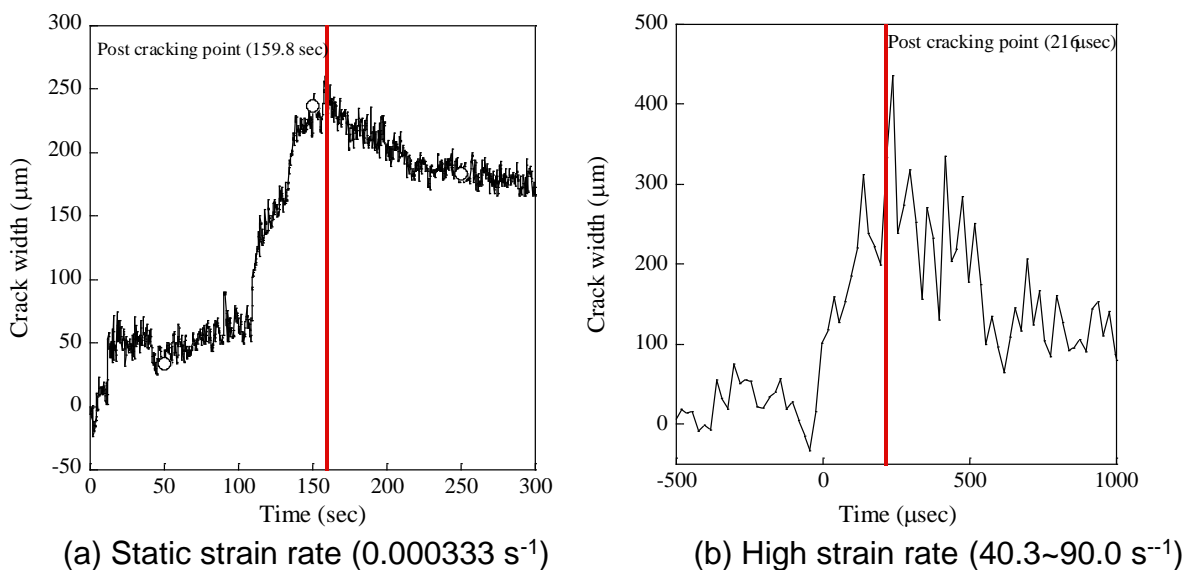


Fig. 15 Total width of multiple microcracks excluding a macro crack

6. CONCLUSIONS

The effects of strain rate on multiple microcracking behavior of UHPFRC were investigated at strain rates between 0.000333 and 90.0 s^{-1} using the DIC technique. Based on the experimental results, the following conclusions are drawn.

- The multiple microcracking behavior of all UHPFRC specimens (0.5–2.0 vol% smooth steel fibers) under tensile load was clearly observed using the DIC analysis.
- The propagation and width of each microcrack was observed in detail via the DIC analysis.
- A suitable subset size for the DIC analysis was determined by selecting the target standard deviation error (0.005 pixel) of displacement based on the SSSIG value and variance of image noise.
- The standard deviation error ($\sigma(\Delta u) = 1.76 \mu\text{m}$, $\sigma(\Delta v) = 2.02 \mu\text{m}$) of displacement at high strain rates (40.3–90.0 s^{-1}), determined using a high-speed camera with resolution of 256×128 pixels, was found bigger than that ($\sigma(\Delta u) = 0.14 \mu\text{m}$, $\sigma(\Delta v) = 0.17 \mu\text{m}$) at the static strain rate (0.000333 s^{-1}), determined using a charge-coupled device camera with resolution of 2336×1752 pixels, because of the lower image resolution of the high-speed camera.
- Irrespective of the applied strain rate, the multiple microcracks were generated prior to the post-cracking point; however, there were no additional microcracks created after the post-cracking point.
- The UHPFRC specimens with low fiber content (0.5–1.0 vol%) generated faster crack percolation ($\Delta t = 2.2\text{--}15.2 \text{ s}$), whereas those with higher fiber contents (1.5–2.0 vol%) took longer ($\Delta t = 35.0\text{--}57.4 \text{ s}$) for the coalescence and percolation of microcracks.
- At the static strain rate (0.000333 s^{-1}), the average crack width increased from 33.5 to 55.7 μm as the fiber volume content increased from 1.0 to 2.0 vol%. However, at high strain rates (40.3–90.0 s^{-1}), the average crack width decreased from 171 to 114 μm as the fiber volume content increased from 1.0 to 2.0 vol%.
- Irrespective of the applied strain rate, the total width (between 45 and 210 μm) of multiple microcracks (with the exception of the major crack) was maintained or it decreased slightly during major crack opening.

REFERENCES

- Thomas R.J. and Sorensen A.D. (2017) "Review of strain rate effects for UHPC in tension", *Constr. Build. Mater.*, **153**, 846-856.
- Naaman A.E. and Reinhardt H.W. (1996) "Characterization of high-performance fiber-reinforced cement composites-HPFRCC", *RILEM Proc.* **31**, 1–24.
- Park S.H., Kim D.J., Ryu G.S., and Koh K.T. (2012) "Tensile behavior of ultra-high-performance hybrid fiber-reinforced concrete", *Cem. Concr. Compos.*, **34**, 172–184.
- Wille K., El-Tawil S., and Naaman A.E. (2014) "Properties of strain hardening ultra-high-performance fiber-reinforced concrete (UHP-FRC) under direct tensile loading", *Cem. Concr. Compos.*, **48**, 53–66.
- Tran T.K. and Kim D.J. (2014) "High strain rate effects on direct tensile behavior of high-performance fiber-reinforced cementitious composites", *Cem. Concr. Compos.*, **45**, 186–200.
- Tran N.T., Tran T.K., and Kim D.J. (2015) "Direct tensile response of ultra-high-performance fiber-reinforced concretes at high strain rates", *Cem. Concr. Res.*, **69**, 72–87.
- Park S.H., Kim D.J., and Kim S.W. (2016) "Investigating impact resistance of ultra-high-performance fiber-reinforced concrete using an improved strain energy frame impact machine", *Constr. Build. Mater.*, **125**, 145–159.

— **Proceeding Paper**

- Park J.K., Kim S.W., and Kim D.J. (2017) "Matrix-strength-dependent strain-rate sensitivity of strain hardening fiber-reinforced cementitious composites under tensile impact", *Compos. Struct.* **162**, 313–324.
- Chu T.C., Ranson W.F., Sutton M.A., and Peters W.H. (1985) "Applications of digital image correlation techniques to experimental mechanics", *Exp. Mech.*, **25**, 232–244.
- Destrebeeq J.F., Toussaint E., and Ferrier E. (2011) "Analysis of cracks and deformations in a full-scale reinforced concrete beam using a digital image correlation technique", *Exp. Mech.*, **51**, 879–890.
- Gencturk B., Kossain K., Kapadia A., Labib E., and Mo Y.L. (2014) "Use of digital image correlation technique in full-scale testing of prestressed concrete structures", *Measurement*, **47**, 505–515.
- Choi S. and Shah S.P. (1997) "Measurement of deformations on concrete subjected to compression using image correlation", *Exp. Mech.* **37**, 307–313.
- Yoneyama S., Morimoto Y., and Takashi M. (2006) "Automatic evaluation of mixed-mode stress intensity factors utilizing digital image correlation", *Strain* **42**, 21–29.
- Shah S.G. and Chandra Kishen J.M. (2011) "Fracture properties of concrete–concrete interfaces using digital image correlation", *Exp. Mech.* **51**, 303–313.
- Wu Z., Rong H., Zheng J., Xu F., and Dong W. (2011) "An experimental investigation on the FPZ properties in concrete using digital image correlation technique", *Eng. Fract. Mech.*, **78**, 2978–2990.
- Choi S., Lim B., Oh C.K., and Joh C. (2012) "Technique for the measurement of crack widths at notched/unnotched regions and local strains", *J. Korea Concr. Inst.*, **24**, 205–214.
- Forquin P. (2012) "An optical correlation technique for characterizing the crack velocity in concrete", *Eur. Phys. J.: Spec. Top.* **206**, 89–95.
- Gao G., Yao W., Xia K., and Li Z. (2015) "Investigation of the rate dependence of fracture propagation in rock using digital image correlation (DIC) method", *Eng. Fract. Mech.*, **138**, 146–155.
- Pyo S., Alkaysi M., and El-Tawil S. (2016) "Crack propagation speed in ultra-high-performance concrete (UHPC)", *Constr. Build. Mater.*, **114**, 109–118.
- Yaofeng S. and Pang J.H.L. (2007) "Study of optimal subset size in digital image correlation of speckle pattern image", *Opt. Lasers Eng.*, **45**, 967–974.
- Pan B., Xie H., Wang Z., Qian K., and Wang Z. (2008) "Study on subset size selection in digital image correlation for speckle patterns", *Opt. Express*, **16**(10), 7037–7048.